Energy Engineering

Tech Science Press

https://doi.org/10.32604/ee.2026.076567

ARTICLE

Improved WOA-Based Multilevel Resource Coordinated Scheduling Strategy for Active Distribution Network

Rongyi Niu[1,2], **Chong Li**[1,2,*], **Gang Gu**[1,2] **and Qunhui Hu**[1,2]

[1]NARI Technology Co., Ltd., Nanjing, China
[2]NARI Nanjing Control System Co., Ltd., Nanjing, China

*Corresponding Author: Chong Li. Email: chongli20232@163.com

Received: 22 November 2025; Accepted: 09 January 2026; Published: 12 November 2026

ABSTRACT: To address the operational complexity caused by the high proportion of new energy integration into distribution networks, a multilevel resource-coordinated operation strategy based on an improved whale optimization algorithm (improved WOA) is proposed for active distribution networks (ADNs). A bilevel optimization model is established to ensure the economic and safe operation of ADNs. The upper level is used to minimize the total system operation cost, while the lower level is used to optimize the power balance. Subsequently, the improved WOA, integrated with an adaptive weight and chaotic disturbance mechanisms, is used to solve the bilevel model and obtain a multi-resource coordinated operation strategy. This framework can help to enhance convergence and avoid local optima. In the simulation section, the IEEE 33-bus system is used to test the performance of the multilevel resource coordinated operation strategy. The simulation results reveal that the proposed approach can reduce the total system operation cost to 9.72×10^4 CNY. Moreover, the fossil fuel consumption of the diesel generator and the charging cost of electric vehicles are reduced by 15% and 18%, respectively. In addition, the power supply–demand matching accuracy is increased to 99.8%. Compared with the multi-element heuristic algorithm, the improved WOA shows significant superiority and robustness. This research provides an economical and stable multi-resource coordinated scheduling solution for distribution networks with a high proportion of renewable energy.

KEYWORDS: Active distribution network; multilevel resources; whale optimization algorithm; comprehensive scheduling

1 Introduction

With the rapid development of distributed resources such as photovoltaics (PV) and energy storage systems (ESS), the control and optimization of active distribution networks formed by integrating these resources have become key research areas [1–3]. Distributed resources, such as PVs, exhibit distinct output characteristics across scenarios and time periods, featuring significant volatility and variability, which pose considerable challenges for the coordinated optimization of various resources [4–6]. Related research has indicated that the coordinated control of distribution networks with distributed resources is difficult. Given the inherent electrical characteristics of distribution networks and the output volatility of distributed resources, the coordinated optimization of integrating distributed resources into distribution networks has become an urgent problem [7–9].

In recent years, scholars have extensively researched and analyzed the coordinated optimization of distributed resources [10–13]. In terms of scheduling frameworks, bi-level or multi-objective models

Copyright © 2027 The Authors. Published by Tech Science Press. This work is licensed under a Creative Commons Attribution 4.0 International License, which permits unrestricted use, distribution, and reproduction in any medium, provided the original work is properly cited.

are widely used to address multi-agent collaboration problems. Turan et al. [14] introduced distributed algorithms based on primal-dual optimization that were resilient to Byzantine attackers and converged to a near-optimal solution. Su et al. [15] proposed a bilevel optimization model for ADNs that integrates hybrid wind-solar-hydrogen-storage systems. An electro-hydrogen coupling framework was constructed, and the volatility of wind and solar output was modelled using a copula function. Chen et al. [16] proposed an active distribution network multi-objective optimization scheduling method in which the peak–valley difference of the system load was reduced by optimizing the electric vehicle load. Xiao et al. [17] proposed a two-layer optimal scheduling strategy to address the overvoltage problem in high-photovoltaic power-penetrated distribution networks. The proposed scheduling strategy included an autonomous optimization layer and a coordination optimization layer, and a min–max robust game model and a mixed-integer second-order cone programming-based model were proposed to minimize the operating costs of PV stakeholders and power utility stakeholders, respectively.

Multilevel resource coordination is the key to releasing the operational potential of ADNs, and its core lies in tapping the complementary characteristics of different resources. As a core hub for mitigating volatility and peak shaving-valley filling, ESSs have increased rapidly from 12 GW in 2020 to 52 GW in 2024 [18]. Ma et al. [19] proposed an energy management strategy based on deep learning for grid-forming energy storage systems. Still, it lacked a full-scenario coupling of multilevel resources and failed to fully consider the load regulation potential of orderly electric vehicle (EV) charging and the base-load support role of coal-fired power units. Qi et al. [20] proposed a genetic algorithm-based optimization configuration for energy storage in electric networks; however, traditional optimization algorithms usually suffer from slow convergence and a tendency to fall into local optima in high-dimensional scheduling problems, making them challenging to balance the dual objectives of economic stability. Li et al. [21] proposed a global centralized dispatch model that applied battery energy storage system technology to ADN with a renewable energy source, aiming to minimize the power purchase cost while considering the network active loss cost and the voltage deviation penalty cost. Nevertheless, this method did not sufficiently explore the collaborative mechanism between power balance constraints and cost optimization, nor did it consider the ESSs' limit on the rate of change of charge–discharge power, leading to a disconnect between theoretical schemes and engineering practices [22].

Despite the significant progress offered by existing research, when complex distribution network scheduling scenarios involving multiple heterogeneous resources are considered, existing scheduling strategies still have room for improvements in solution efficiency, global optimization capability, and the guarantee of refined control over system power balance. To address this research issue, a multilevel resource coordinated operation strategy based on the improved whale optimization algorithm (improved WOA) is proposed. First, mathematical models are established for PV, wind power, ESSs, EVs, and diesel generators to characterise their physical and operational characteristics accurately. Furthermore, a bilevel coordinated scheduling model is established with dual objectives: minimizing the total system operating cost and optimizing the power balance. Finally, the traditional WOA is improved by introducing an adaptive weight mechanism and a chaotic disturbance mechanism, resulting in an improved WOA with better optimization performance. The effectiveness and superiority of the improved WOA method are verified by comparing it with other algorithms, including WOA, chaotic WOA (CWOA), adaptive WOA (AWOA), particle swarm optimization (PSO), and the genetic algorithm (GA), applied to the IEEE 33-bus system. The main contributions of this paper are as follows.

(1) A refined multilevel resource scheduling model is constructed with photovoltaics, wind turbines, energy storage systems, electric vehicles, and diesel generators, while fully considering their physical constraints and operation costs.

(2) To address the shortcomings of the basic WOA, an adaptive weight mechanism and a chaotic disturbance mechanism are innovatively employed, and the improved WOA is proposed. This effectively balances the algorithm's global exploration and local exploitation capabilities, accelerates convergence, and prevents premature convergence.

(3) A bilevel scheduling model is established to minimize the total operating cost of the system and optimize the power balance. Simulations of the IEEE 33-bus standard system are presented, and extensive discussions are provided.

2 Multilevel Resources

The efficient coordination of multilevel resources forms the foundation for active distribution networks to operate safely, stably, and economically. Accurately characterizing the physical properties and operational constraints of various resources is the primary prerequisite for constructing an efficient coordinated scheduling model. In this section, the mathematical models for the five key resources involved in coordinated optimization are systematically established, laying a foundation for the subsequent development of the bilevel optimization model. The overall composition relationship is shown in Fig. 1.

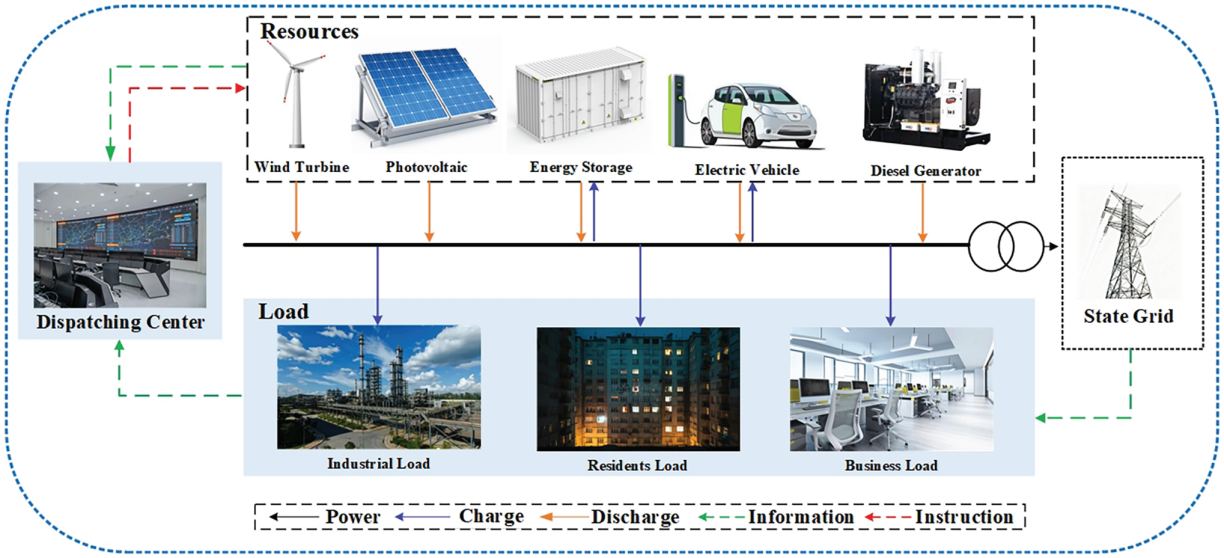


Figure 1: Multilevel resource architecture of the active distribution network.

2.1 Photovoltaic Power Generation Model

Photovoltaic power generation directly converts sunlight into electrical energy via the photovoltaic effect at semiconductor interfaces. A standard system configuration encompasses solar panels, controllers, and inverters, all of which are primarily composed of electronic components. The manufacturing procedure involves serially connecting solar cells, encapsulating them into protected modules, and assembling these modules with controllers and inverters to form a functional power generation unit. The formula for calculating the photovoltaic power generation output is as follows:

$$P_{PV} = \frac{\mathrm{d}X}{3.6 \times \mathrm{d}t} \times S \times \eta_{PV} \tag{1}$$

where X is the hourly solar radiation intensity on a typical day, S is the area of the PV array, P_{PV} is the hourly power generation output on a typical day, η_{PV} is the PV efficiency, and t is the illumination time. When dt is infinitely close to 0, the characteristic curve of the real-time smooth power generation output is obtained.

The comparison curve between the daily output power and the radiation intensity measured at a photovoltaic power station is shown in Fig. 2. The variation trends of the solar radiation intensity curve and the photovoltaic power generation curve are essentially the same. Power generation fluctuates in parallel with irradiance fluctuations. In addition, Fig. 2 shows that the day's maximum output power occurs at 14:30, with a corresponding irradiance of 1145 W/m^2 and an output power of 97.2 kW. Moreover, during the 10-min (13:10 to 13:20) sampling interval, which corresponds to a significant irradiance fluctuation, the maximum fluctuation in the DC-side output power of the photovoltaic power station can reach 92.6 kW, approximately 90% of the maximum output power.

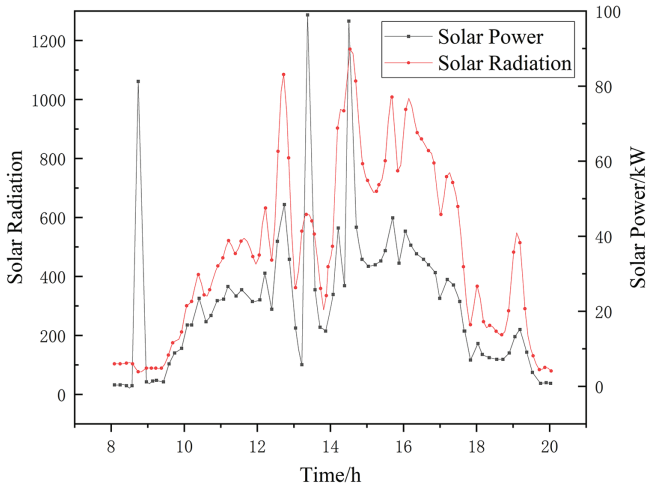


Figure 2: Comparison of daily output power and radiation intensity.

2.2 Wind Power Generation Model

Wind energy, as the raw form for wind power generation, is classified as renewable energy. It is abundant and almost inexhaustible; thus, it is widely used in China. Owing to its prominent environmental friendliness, wind power generation plays a key role in alleviating power shortages. Moreover, benefiting from the policy support of the on-grid electricity price, it has achieved rapid growth in recent years.

Within the system, the wind turbine (WT) initially captures and converts wind energy into mechanical energy. This mechanical energy is then transferred by the transmission system, which incorporates components such as gearboxes, to the generator. Operating on the principle of electromagnetic induction, the generator converts electrical energy into mechanical energy. The resulting alternating current is rectified into direct current to accommodate diverse power requirements. Furthermore, the pitch angle control system optimizes energy capture and conversion efficiency by adjusting the blade angle. In contrast, the power control system ensures the generator's stable operation across varying wind speeds, thereby guaranteeing the reliability of the power output. Through the coordinated operation of these components, the wind power system efficiently transforms wind energy into clean electricity for grid integration.

The active power output of a WT is predominantly governed by wind speed. The WT is activated once the wind speed reaches the cut-in value. Within the operational range between the cut-in and rated wind speeds, the output power follows a parabolic profile with respect to the wind speed. However, the

WT is automatically shut down to prevent structural damage when the wind speed surpasses the cut-out threshold. The corresponding mathematical representation of the output power is provided in Eq. (2), and the characteristic power curve of the wind power system is depicted in Fig. 3.

$$P_{WT} = \begin{cases} 0 & v < v_{in} \\ P_{WT,N}\frac{(v-v_{in})}{(v_N-v_{in})} & v_{in} < v < v_N \\ P_{WT,N} & v_N < v < v_{out} \end{cases} \quad (2)$$

where v represents the actual wind speed, v_{in} represents the cut-in wind speed, v_N represents the rated wind speed, v_{out} represents the cut-out wind speed, and $P_{WT,N}$ represents the rated power.

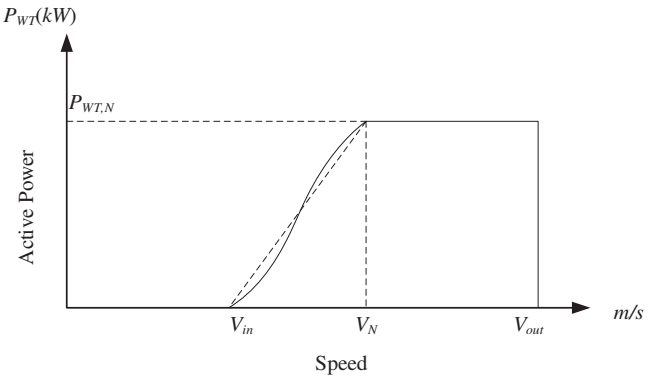


Figure 3: Relationship between the active power and the wind speed of the WT.

2.3 Energy Storage Model

In terms of different ESS forms, they can be divided into electrochemical ESS (such as lithium-ion batteries and lead–acid batteries), mechanical ESS (such as pumped storage and flywheel energy storage), and electromagnetic ESS (such as supercapacitors and superconducting energy storage). The characteristics of the various ESS types are compared in Table 1.

Table 1: Comparison of the characteristics of various types of energy storage.

Type	Power Density (kW/kg)	Energy Density (kWh/kg)	Charge–Discharge Efficiency (%)	Cycle Life (Times)
Lithium-ion battery ESS	0.1–0.5	0.05–0.2	85–95	3000–10,000
Lead-acid battery ESS	0.05–0.2	0.02–0.05	75–85	500–1500
Pumped storage	0.01–0.05	0.5–5.0	70–85	10,000+
Flywheel ESS	5–50	0.005–0.02	85–95	100,000+
Supercapacitor	1–10	0.001–0.005	90–98	1,000,000+

Given that the research object of this paper is resource collaboration at the distribution network level, the ESS needs to exhibit fast response, flexible installation, and high efficiency. Therefore, a lithium-ion battery ES is selected as the research object.

The state of charge (SOC) of the ESS represents the proportion of the currently stored electrical energy to the rated capacity. Its dynamic change equation is as follows:

$$SOC(t) = SOC(t-1) - \frac{P_{ESS}(t) \cdot \Delta t}{E_{ESS,N}} \tag{3}$$

where $SOC(t)$ is the SOC value of the ESS at time t; Δt is the time step; $E_{ESS,N}$ is the rated capacity of the ESS; and $P_{ESS}(t)$ is the charge–discharge power of the ESS at time t.

The safe operation and service life of the ESS are subject to the following charge–discharge power and SOC constraints:

$$-P_{ESS,N} \cdot \eta_{dis} \le P_{ESS}(t) \le P_{ESS,N} \cdot \eta_{ch} \tag{4}$$

$$SOC_{\min} \le SOC(t) \le SOC_{\max} \tag{5}$$

When $P_{ESS}(t)$ is positive, it indicates charging; when it is negative, it indicates discharging. $P_{ESS,N}$ is the rated power of the ESS, η_{ch} and η_{dis} are the charging efficiency and discharging efficiency, respectively, and $SOC_{\min}$ and $SOC_{\max}$ are the minimum and maximum SOC limits, respectively.

In addition, to avoid the shortening of service life caused by frequent charging and discharging of ES, the change rate of charge and discharge power must be limited:

$$-r_{ESS} \cdot P_{ESS,N} \le P_{ESS}(t) - P_{ESS}(t-1) \le r_{ESS} \cdot P_{ESS,N} \tag{6}$$

where r_{ESS} is the power change rate limit.

2.4 Electric Vehicle Model

The charging load of EVs can be divided into two categories: disorderly and orderly. Their mathematical models are as follows.

Disorderly charging means that after the user connects the EV to the charging pile, charging proceeds at the maximum power until the battery is fully charged. Its charging power $P_{EV,dis}(i,t)$ is as follows:

$$P_{EV,dis}(i,t) = \begin{cases} P_{EV,\max}(i), & t \in [t_{start}(i), t_{end}(i)] \\ 0, & \text{others} \end{cases} \tag{7}$$

where i is the number of EVs, $P_{EV,max}(i)$ is the maximum charging power of the i-th EV, $t_{start}(i)$ is the charging start time of the i-th EV, and $t_{end}(i)$ is the charging end time of the i-th EV. The total disorderly charging load of N EVs in the system is as follows:

$$P_{EV,dis}(t) = \sum_{i=1}^{N} P_{EV,dis}(i,t) \tag{8}$$

Orderly charging is a strategy in which, while satisfying the user's prescribed charging demand, an optimization algorithm adjusts the initiation time and power level of charging sessions to shift the aggregate load away from grid peak periods. The mathematical formulation of this strategy is subject to the following constraints:

Charging demand constraint: The final SOC is equal to the target value.

$$SOC_{init}(i) + \frac{\sum_{t=t_{start}(i)}^{t_{end}(i)} P_{EV,ord}(i,t) \cdot \Delta t \cdot \eta_{EV}}{E_{EV}(i)} \geq SOC_{target} \tag{9}$$

where $SOC_{init}(i)$ is the initial SOC of the i-th EV, $P_{EV,ord}(i,t)$ is the orderly charging power of the i-th EV at time t, η_{EV} is the charging efficiency of the EV, $E_{EV}(i)$ is the battery capacity of the i-th EV, and SOC_{target} is the target SOC of the i-th EV.

Charging power constraint: The charging power shall not exceed the maximum charging power.

$$0 \leq P_{EV,ord}(i,t) \leq P_{EV,\max}(i,t) \tag{10}$$

The total orderly charging load of N EVs in the system is as follows:

$$P_{EV,ord}(t) = \sum_{i=1}^{N} P_{EV,ord}(i,t) \tag{11}$$

2.5 Diesel Generator Model

Diesel generators (DGs), as traditional energy generation equipment, have the advantages of flexible installation, compact size, long service life, and easy maintenance and inspection compared with large-scale thermal power plants. However, they face significant challenges regarding emissions and environmental impacts. The characteristics of fast startup, simple operation, and high durability enable DGs to be used throughout industrial, commercial, and household emergency power supply scenarios. When the power supply units are generating wind and PV power, although they have low pollution levels, the outputs of these renewable energy sources exhibit some randomness. They may fail to meet the electricity demand continuously. DGs can provide stable and reliable power support; thus, they remain essential backup power sources in scenarios requiring an uninterrupted power supply.

The power generation cost of DGs is as follows:

$$C_{DG} = aP_{DG}^2 + bP_{DG} + c \tag{12}$$

where P_{DG} is the power output of the DGs, and a, b, and c are the cost coefficients for fuel combustion.

3 Bilevel Scheduling Model and Improved WOA

3.1 Bilevel Optimal Scheduling Model

A bilevel optimal scheduling framework is proposed, as illustrated in Fig. 4. An upper-level model is formulated to minimize the total operational cost of the distribution network. By integrating the cost functions and operational constraints of multilevel resources, it generates optimal schedule strategies. These strategies, which include optimized load and resource output profiles, are subsequently passed to the lower-level model. The primary focus of the lower level is to evaluate the power balance by comparing the aggregated resource output with the actual load demand across each time interval. It quantifies any imbalance and feeds this information back to the upper level if deviations exceed permissible limits. The IWOA then iteratively refines the solution based on this feedback until the coordinated optimal operation strategy is ultimately derived.

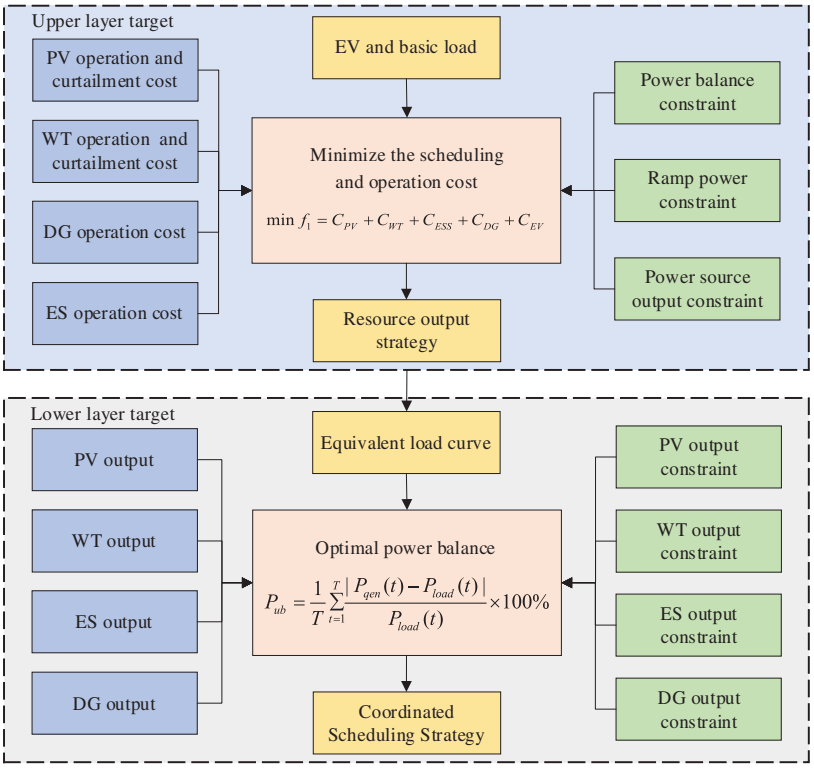


Figure 4: Bilevel optimal scheduling model.

3.1.1 Objective Function

Upper-level target: The scheduling and operating costs of the distribution network are minimized. The operation cost includes both traditional and renewable energy power generation. The objective function can be written as follows:

$$\min f_1 = C_{PV} + C_{WT} + C_{ESS} + C_{DG} + C_{EV} \tag{13}$$

$$C_{PV} = C_{PV}^{bace} + \lambda_{PV} P_{PV}^{*} \tag{14}$$

$$C_{WT} = C_{WT}^{bace} + \lambda_{WT} P_{WT}^{*} \tag{15}$$

where C_{PV} is the operation cost of PV power generation, including the basic operation and maintenance cost of PV and the curtailment cost of PV; C_{PV}^{bace} is the basic operation and maintenance cost of PV; P_{PV}^{*} is the photovoltaic curtailment power; λ_{PV} is the photovoltaic curtailment coefficient (set to 0.7); C_{WT} is the operation cost of wind power generation, including the basic operation and maintenance cost of wind power and the wind curtailment cost; C_{WT}^{bace} is the basic operation and maintenance cost of wind power; P_{WT}^{*} is the wind curtailment power; λ_{WT} is the wind curtailment coefficient, set to 0.8; C_{ESS} is the operation cost of the ESS; C_{DG} is the power generation cost of the DGs, and C_{EV} is the charging cost of EVs.

Lower-level target: The power balance is taken as the optimization objective, and the power imbalance index P_{ub} is defined. Based on the resource scheduling benchmark curve output by the upper model, the power supply and demand deviations at each moment are minimized by dynamically adjusting ESS power and DG fine-tuning power, ensuring the safe and stable operation of the system. The calculation formula is as follows:

$$P_{ub} = \frac{1}{T}\sum_{t=1}^{T}\frac{|P_{gen}(t) - P_{load}(t)|}{P_{load}(t)} \times 100\% \tag{16}$$

$$P_{gen}(t) = P_{PV}(t) + P_{WT}(t) + P_{ESS}(t) + P_{DG}(t) \tag{17}$$

$$P_{load}(t) = P_{base}(t) + P_{EV}(t) \tag{18}$$

where T is the total number of time periods in the scheduling cycle, $P_{gen}(t)$ is the total power generation of the system at that time, and $P_{load}(t)$ is the total system load power at that time. If P_{ub} exceeds the threshold, it is fed back to the upper cost function as a penalty term.

3.1.2 Constraint Conditions

(1) Power Balance Constraint

The output power of each unit in the distribution network must match the load to maintain supply–demand balance. The load includes the EV charging load and the base load. Any deviation between them will cause a power surplus or shortage, which is unfavourable to the stable operation of the distribution network. The formula is as follows:

$$P_{PV} + P_{WT} + P_{ESS} + P_{DG} - P_{EV} - P_{base} = 0 \tag{19}$$

where P_{PV}, P_{WT}, P_{ESS}, and P_{DG} are the powers of the PV, WT, ESS, and DGs, respectively; P_{EV} is the charging load power of the EVs, and P_{base} is the base electricity load power. ESS adjusts P_{ESS} by real-time charging and discharging. When $P_{ESS} > 0$, the ESS charge absorbs the surplus power when $P_{ESS} < 0$, the discharge supplements the power gap to ensure that the power balance constraint is satisfied.

(2) Ramp Power Constraint

DGs are prone to overload when the load increases suddenly or when the power output increases rapidly. To prevent this situation from affecting the operational stability of DGs, the corresponding ramp power constraint is set. The formula is as follows:

$$R_{t,down}^{DG}\Delta t \le P_t^{DG}(t) - P_t^{DG}(t-1) \le R_{t,up}^{DG}\Delta t \tag{20}$$

where $R_{t,down}^{DG}\Delta t$ and $R_{t,up}^{DG}\Delta t$ are the upper and lower ramp rates of the DGs, respectively.

(3) Power Source Output Constraint

When a power source is connected to the distribution network to participate in optimal scheduling, its upper and lower limits must be constrained to avoid exceeding the limits. The formulae are as follows:

$$P_{PV}^{\min} \le P_{PV} \le P_{PV}^{\max} \tag{21}$$

$$P_{WT}^{\min} \le P_{WT} \le P_{WT}^{\max} \tag{22}$$

$$P_{ESS}^{\min} \le P_{ESS} \le P_{ESS}^{\max} \tag{23}$$

$$P_{DG}^{\min} \le P_{DG} \le P_{DG}^{\max} \tag{24}$$

where $P_{PV}^{\min}$ and $P_{PV}^{\max}$ represent the upper and lower limits of the PV output, respectively, $P_{WT}^{\min}$ and $P_{WT}^{\max}$ represent the upper and lower limits of the wind power output, respectively; $P_{ESS}^{\min}$ and $P_{ESS}^{\max}$ represent the upper and lower limits of the ESS output, respectively; and $P_{DG}^{\min}$ and $P_{DG}^{\max}$ represent the upper and lower limits of the DG output, respectively.

3.2 Improved Whale Optimization Algorithm

The WOA is a nature-inspired heuristic algorithm proposed by Mirjalili and Lewis in 2016 that mimics the unique bubble-net foraging strategy of humpback whales. The whales hunt krill and small fish by creating spiralling bubbles in a circular or '9'-shaped path to trap their prey, a behaviour exclusive to this species. In this work, this spiral bubble-net feeding mechanism is mathematically modelled to address optimization problems. It is undeniable that the traditional WOA suffers from a slow convergence speed and a tendency to become trapped in local optima. To solve this problem, an IWOA was designed. An adaptive weight mechanism and a chaotic disturbance mechanism are introduced. These mechanisms improve the speed and accuracy of the search. The algorithm's performance is further balanced.

The bubble-net foraging behaviour of humpback whales is algorithmically abstracted into three key phases: exploration, exploitation, and prey encircling. The encircling phase, a specific mechanism within exploitation, operates under the premise that the current best candidate solution represents the target prey or is proximate to the global optimum. Once this best search agent is identified, all the other agents update their positions to move closer to it. The following equations mathematically represent this collective movement:

$$\vec{D} = \left| \vec{C} \times \vec{X^*}(t) - \vec{X}(t) \right| \tag{25}$$

$$\vec{X}(t+1) = w \cdot \left(\vec{X^*}(t) - \vec{A} \cdot \vec{D} \right) + (1-w) \cdot \vec{X}(t) \tag{26}$$

where t is the current iteration number, $\vec{A}$ and $\vec{C}$ are coefficient vectors, $\vec{X^*}(t)$ is the position vector of the best solution obtained thus far, and $\vec{X}(t)$ is the current position vector. If a better solution is available, $\vec{X^*}(t)$ should be updated in each iteration. The calculation processes of vectors $\vec{A}$ and $\vec{C}$ are as follows:

$$\vec{A} = 2\vec{k} \cdot \vec{r} - \vec{k} \tag{27}$$

$$\vec{C} = 2 \cdot \vec{r} \tag{28}$$

where $\vec{r}$ is a random value between [0, 1] and k is an adaptive parameter. It is expressed as follows:

$$k = 2 - t \times \frac{2}{T} \tag{29}$$

where t is the current number of iterations and T is the maximum number of iterations. The value range of k is linearly reduced from 2 to 0. The expression of the adaptive weight w is as follows:

$$w = 0.4 + t \times \frac{1}{2T} \tag{30}$$

where w is the weight that increases linearly with the number of iterations, its value range is increased from 0.4 to 0.9 [23].

During the exploitation phase (simulating a bubble-net attack), humpback whales employ two concurrent strategies: a shrinking encircling mechanism and a spiral position update. Shrinking encircling is achieved by decreasing the value of the parameter k, which in turn reduces the coefficient vector $\vec{A}$. This contraction confines the new position of a search agent to a hypersphere centered on the search agent's original location and with radius equal to the distance to the current best agent.

The spiral position update mechanism first calculates the distance between the whale at (X, Y) and the prey at (X^*, Y^*) and then creates k spiral equations between the whale and the prey to imitate the spiral movement of humpback whales as follows:

$$\vec{X}(t+1) = w \cdot \left(\vec{D'} \cdot e^{ql} \cdot \cos(2\pi l) + \vec{X^*}(t)\right) + (1-w) \cdot \vec{X}(t) \tag{31}$$

where $\vec{D'}$ is the distance between the i-th whale and the prey, q is a constant defining the shape of the logarithmic spiral, and l is a random number between [−1, 1].

Notably, humpback whales concurrently employ shrinking encircling and spiral paths during a bubble-net attack. To emulate this synchronous behaviour, the algorithm assumes an equal probability of selecting either the shrinking encircling mechanism or the spiral update model at each iteration to update a whale's position. This probabilistic selection is mathematically represented as follows:

$$\vec{X}(t+1) = \begin{cases} w \cdot \left(\vec{X^*}(t) - \vec{A} \cdot \vec{D}\right) + (1-w) \cdot \vec{X}(t) & p \le 0.5 \\ w \cdot \left(\vec{D'} \cdot e^{ql} \cdot cos(2\pi l) + \vec{X^*}(t)\right) + (1-w) \cdot \vec{X}(t) & p > 0.5 \end{cases} \tag{32}$$

where p is a random number between [0, 1].

In accordance with the bubble-net method, humpback whales also engage in a random search for prey, which is modelled as the exploration phase. In this phase, a search agent updates its position based on a randomly selected counterpart rather than the best-known solution, thereby promoting population diversity. This behaviour is mathematically implemented by enforcing $|L| > 1$, which compels the agent to diverge from the current best solution and explore broader regions of the search space. This mechanism is crucial for enhancing the IWOA's global search capability and can be written as follows:

$$\vec{D} = \left|\vec{C} \times \vec{X}_{rand} - \vec{X}(t)\right| \tag{33}$$

and

$$\vec{X}(t+1) = w \cdot \left(\vec{X}_{rand} - \vec{A} \times \vec{D}\right) + (1-w) \cdot \vec{X}(t) \tag{34}$$

Finally, the logistic chaotic map is introduced. A sequence with chaotic characteristics is generated. The population diversity is increased by:

$$z_{t+1} = m \cdot z_t \cdot (1 - z_t) \tag{35}$$

where m is a control parameter, and it is set to 3.9 to ensure that the characteristics are chaotic [24]. z_t is the chaotic value at the t-th iteration. The initial value is 0.5. Thus, the disturbed position can be updated as follows:

$$X'(t) = X(t) + 0.01 \times z_t \left(x_{\max} - x_{\min}\right) \cdot r \tag{36}$$

where $X'(t)$ is the disturbed position, $x_{\max}$ and $x_{\min}$ are the upper and lower bounds of the search space, respectively.

The IWOA procedure begins with population initialization. Iteratively, each agent updates its position by referencing either a randomly selected peer (when |L| > 1) or the current best solution (when |L| < 1). The a parameter decreases linearly from 2 to 0, whereas w increases from 0.4 to 0.9, dynamically balancing exploration and exploitation. The probability p fine-tunes the position update between spiral and circular motions. A chaotic disturbance is then applied to select individuals, preventing local optima from being trapped. The algorithm terminates once the stopping criterion is met, with the whole procedure detailed in Algorithm 1. The specific process for optimizing the multilevel resource collaborative operation strategy, as proposed in this paper, is shown in Fig. 5.

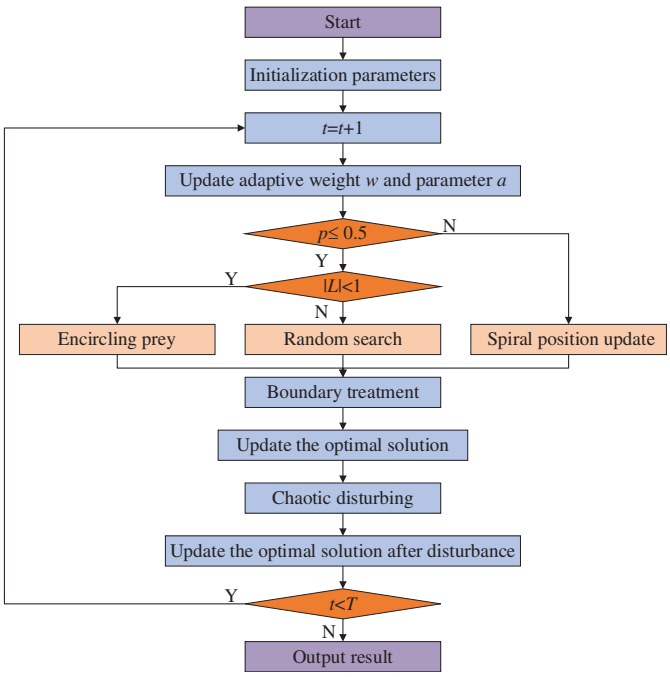


Figure 5: The IWOA optimization process.

Algorithm 1: Improved WOA

Input: objective function $f(x)$, dimension *dim*, search space $[x_{\min}, x_{\max}]$, population size N, and maximum number of iterations T.
Output: optimal solution X^*, optimal fitness function $f(X^*)$.
Initialize the whale population X_i ($i = 1, 2, \ldots, N$), It is randomly generated within $[x_{\min}, x_{\max}]$;
Calculate the fitness $f(X_i)$ of each individual;
Determine the initial optimal solution X^*;
while ($t < T$)
    Calculate the adaptive parameter a and adaptive weight w;
    for each individual from 1 to N;
    Update k, A, C, l, and p;
        if ($p < 0.5$);
            if ($|L| < 1$));
                Update the position of the current search agent by Eq. (31);
            else if ($|L| \geq 1$));
                Select a random search agent (X_{rand});
                Update the position of the current search agent by Eq. (34);
            end if;
        else if ($p > 0.5$);
            Update the position of the current search by Eq. (32);
        end if;
        The boundary of X_i' is processed to ensure that it is in the range of $[x_{\min}, x_{\max}]$;

(Continued)

Algorithm 1 (continued)

Set the probability of chaotic perturbation of X_i';
Calculate $f\left(X_i'\right)$;
if $\left(f\left(X_i'\right) < f\left(X_i\right)\right)$; $X_i = X_i'$;
$f\left(X_i\right) = f\left(X_i'\right)$;
else if $\left(f\left(X_i'\right) > f\left(X_i\right)\right)$; $X^* = X_i$;
$f\left(X^*\right) = f\left(X_i\right)$;
end if;
end for;
Check if any search agent goes beyond the search space and amend it.
Calculate the fitness of each search agent.
Update X^* if there is a better solution.
$(t = t + 1$.
end while;
return X^*.

3.3 Coupling Calculation Process

The bilevel model is solved iteratively. The IWOA operates on the upper-level variable. In each iteration, the lower-level calculates the P_{ub} for the current schedule. A penalty proportional to P_{ub} is added to the upper-level cost function, guiding the IWOA towards solutions that satisfy power balance. The adaptive weight w increases with iterations, focusing the search near promising regions, while the chaotic disturbance periodically diversifies the population. This design promotes convergence toward a high-quality, feasible solution. The specific calculation process is as follows. The coupling mechanism of the bilevel scheduling model is shown in Fig. 6.

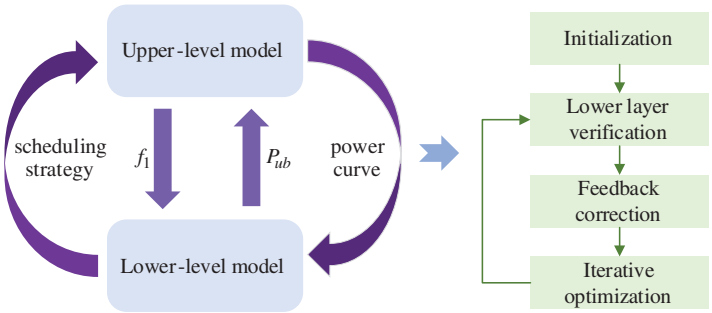


Figure 6: The coupling mechanism of the bilevel scheduling model.

Step 1: The upper model loads the inputs and outputs for the new energy and generates the initial resource-scheduling benchmark curve using IWOA optimization.

$$X_{upper}^0 = \left\{P_{PV}^0, P_{WT}^0, P_{EV}^0, P_{ESS}^0, P_{DG}^0\right\} \tag{37}$$

where X_{upper}^0 is the initial data of the upper-level model, P_{PV}^0, P_{WT}^0, P_{ESS}^0 and P_{DG}^0 are the initial powers of the PV, WT, ESSs, and DGs, respectively; P_{EV}^0 is the initial charging load power of the EVs.

Step 2: The upper reference curve of the k^{th} iteration is input into the lower-level model to obtain the lower adjustment variable X_{lower}^{k} and the corresponding power imbalance index P_{ub}^{k}.

$$X_{lower}^{k} = \left\{\Delta P_{ESS}^{k}, \Delta P_{DG}^{k}\right\} \tag{38}$$

where ΔP_{ESS}^{k} and ΔP_{DG}^{k} are the adjustment variables of the ESS and DGs, respectively.

Step 3: If P_{ub}^{k} is equal to or less than the threshold, then interactive convergence, output X_{upper}^{k} and X_{lower}^{k} as the final scheduling strategy. If P_{ub}^{k} exceeds the threshold, it is fed back to the upper cost function as a penalty term. Update upper-level optimization objectives f_1^*:

$$f_1^* = f_1 + \sigma \cdot P_{ub}^{k} \cdot P_{load} \tag{39}$$

where σ is the penalty coefficient.

Step 4: The penalty upper-level model is re-optimized based on the updated f_1^*, generate X_{upper}^{k+1}, repeat steps 2–4 until convergence.

4 Simulation and Discussion

Based on the IEEE-33 bus system, an active distribution network model with integrated distributed generation and energy storage systems is constructed. A simulation platform is built using MATLAB 2021a. The scheduling cycle is set to 24 h, with a simulation step size of 60 min. Within one simulation step, the load and the output of distributed generation remain unchanged, and the entire cycle is divided into 24 time periods.

Based on the analysis of node-voltage sensitivity [25], selecting voltage weak nodes for accessing new energy can reduce system voltage deviation. The ESS's access to the load center node can shorten the output response distance and reduce the network loss. The DG's access to the core node on the power supply side is convenient for providing stable base-load support. The EV charging load is distributed across the user-side node, which aligns with the actual application scenario. Node selection not only considers system operational efficiency but also aligns with engineering practice. The basic architecture of the IEEE-33 bus system is shown in Fig. 7, and the basic parameters of each resource are shown in Table 2.

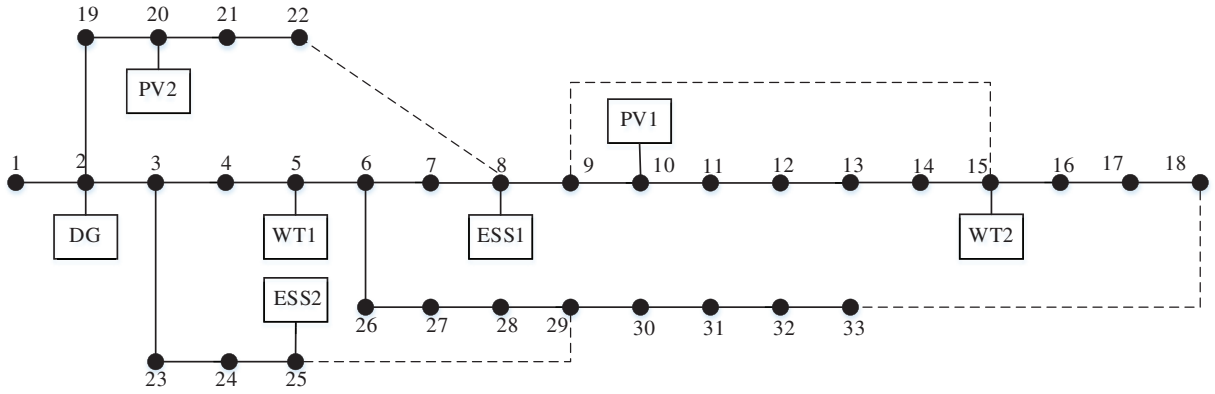


Figure 7: IEEE 33-node topography.

Table 2: Parameter configuration of each resource.

Type of Resources	Connected Nodes	Parameter Names	Parameter Values
PV	10, 20	Photoelectric conversion efficiency (η_{PV})	0.85
		Maximum array area (S)	500 m^2
		Basic operation and maintenance cost (C_{PV}^{base})	0.336 CNY/kWh
		Curtailment coefficient (λ_{PV})	0.7
WT	5, 15	Cut-in wind speed (v_{in})	3 m/s
		Rated wind speed (v_N)	12 m/s
		Cut-out wind speed (v_{out})	25 m/s
		Rated power ($P_{WT,N}$)	200 kW
		Basic operation and maintenance cost (C_{WT}^{base})	0.509 CNY/kWh
		Curtailment coefficient (λ_{WT})	0.8
ESS	8, 25	Rated capacity ($E_{ESS.N}$)	500 kWh
		Rated power ($P_{ESS.N}$)	150 kW
		Charging efficiency (η_{ch})	0.92
		Discharging efficiency (η_{dis})	0.90
		Minimum state of charge ($SOC_{\min}$)	0.2
		Maximum state of charge ($SOC_{\max}$)	0.8
		Power change rate limit ($\Delta P_{ESS,\max}$)	30 kW/min
EV	3-33	Number of vehicles (N)	50 vehicles
		Maximum charging power per vehicle ($P_{EV.N}$)	6.6 kW
		Target state of charge (SOC_{target})	0.8
		Initial state of charge range	0.2–0.5
DG	2	Rated output power ($P_{DG,N}$)	500 kW
		Minimum output power ($P_{DG,\min}$)	150 kW
		Upwards ramp rate ($\Delta P_{DG,up}$)	50 kW/min
		Downwards ramp rate ($\Delta P_{DG,down}$)	30 kW/min
		Power generation cost coefficient (a, b, c)	a = 0.002, b = 0.3, c = 50

4.1 Strategy Selection

Four scheduling optimization scenarios are established in this paper to compare and analyze the role of various scheduling resources in the optimization process. Scenario 1 is the disorderly charging scenario of EVs; Scenario 2 integrates ESS while implementing disorderly EV charging; Scenario 3 is the orderly charging scenario of EVs; and Scenario 4 integrates ESS while implementing orderly EV charging. The control strategies of the four scenarios are shown in Table 3.

Table 3: Multilevel resource collaborative optimization strategy.

Scenario	Disorderly Charging	Orderly Charging	ESS
1	√		
2	√		√
3		√	
4		√	√

The power load curves for orderly and disorderly EV charging are shown in Fig. 8. The comparison reveals that the disorderly charging load fluctuates sharply and exhibits an extremely high peak value, which is prone to causing instantaneous power impacts on the power grid. In contrast, orderly charging, through scheduling optimization, makes the load distribution more uniform and reduces the peak by approximately 20%, effectively suppressing load peaks and facilitating the stable operation of the power grid.

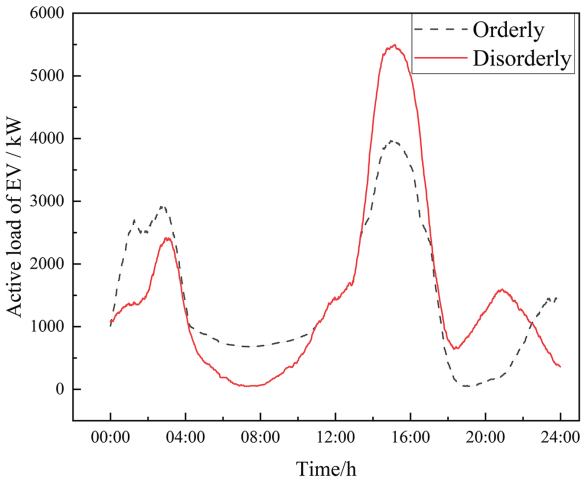


Figure 8: Orderly and disorderly active load of EVs.

The charging and discharging characteristics of ESSs under both orderly and disorderly charging scenarios are shown in Fig. 9. Under disorderly charging, the ESS exhibits significant SOC fluctuations and a deep cycle depth, remaining in the low SOC range near 0.1 for extended periods on multiple occasions, resulting in a long exposure to extreme SOC levels. Under orderly charging, the SOC of ESS changes relatively smoothly with a small cycle depth, and there is no prolonged exposure to extreme SOC levels. It maintains a stable medium-to-high SOC during intermediate periods, thus extending the service life of ESS.

A comparison chart of the optimized load curves for these three scenarios is shown in Fig. 10. Among them, Scenario 4, where EVs adopt orderly charging and ESS participate in optimized scheduling, has the most ideal optimized load curve, with the most significant effects on peak shaving, valley filling, and load curve smoothing. There is a little difference in the capacity of the scheduled resources between Scenario 1 and Scenario 3; however, orderly charging can reduce the peak-valley difference, resulting in Scenario 3 outperforming Scenario 1. Although Scenario 2 integrates the ESS, disorderly charging significantly impairs its regulatory capability. In summary, Scenario 4 is selected as the research scenario for the multilevel resource coordinated operation strategy.

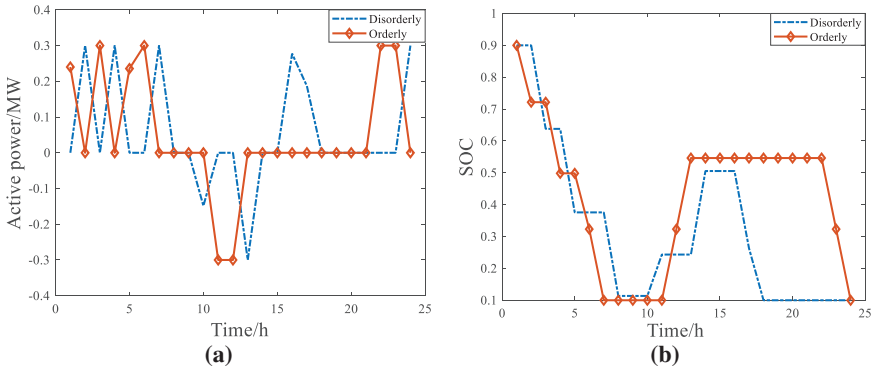


Figure 9: Charging and discharging characteristics of ESSs under both orderly and disorderly charging scenarios: (**a**) Active power of ESS in an orderly and disorderly manner; (**b**) SOC of ESS in an orderly and disorderly manner.

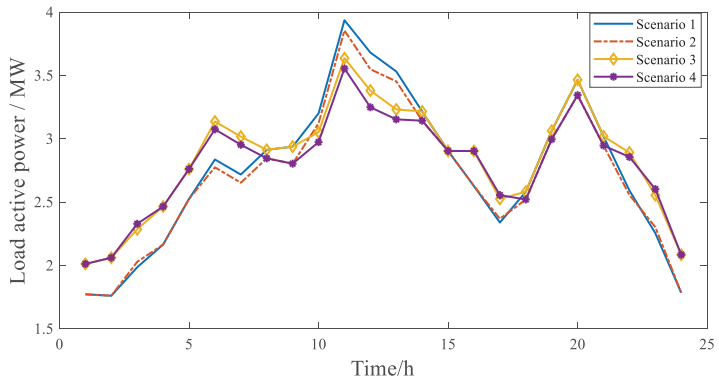


Figure 10: Optimization comparison curve of each scenario.

4.2 Power Balance Analysis

Power balance is the bottom line for the safe operation of distribution networks. In this paper, a multilevel resource scheduling strategy is obtained through the IWOA. The output status of each resource level is shown in Fig. 11, where Fig. 11a presents the output of renewable energy resources and Fig. 11b shows the output of traditional energy resources.

The total supply power of multilevel resource scheduling can be obtained from renewable and traditional energy sources. The total demand power consists of the EV charging load and the power grid's base load.

In this paper, the IWOA achieves high-precision and low-fluctuation power balance through multilevel resource scheduling, as shown in Fig. 12. The maximum power deviation within 24 h is only 5 kW, the average deviation is 1.2 kW, and the supply–demand matching accuracy exceeds 99.8%. Only minor deviations occur in 2 time periods, and the algorithm effectively controls both. The first is during 14:00–14:30, when the PV output rises rapidly, the ESS charging fails to fully respond immediately, resulting in a 3–5 kW surplus. The second is during 18:30–19:00, when PV power is available, and wind power fluctuates, the ramp-up of DGs lags temporarily, causing a 2–3 kW shortage. However, the IWOA controls the deviation within 5 kW by scheduling the ESS to discharge in advance.

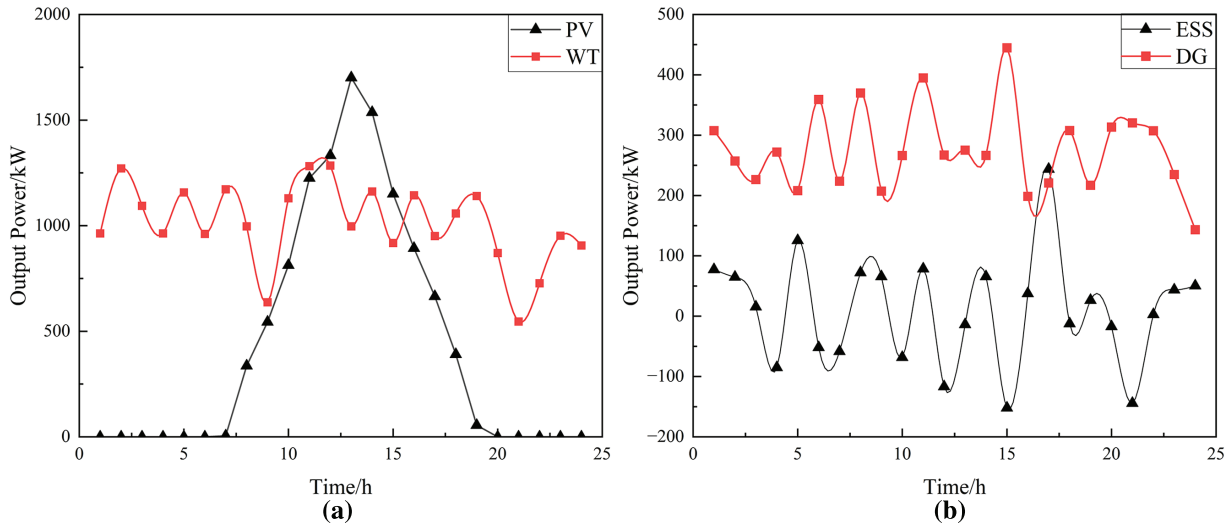


Figure 11: Output status of each resource level: (**a**) Output of renewable resources; (**b**) Output of traditional resources.

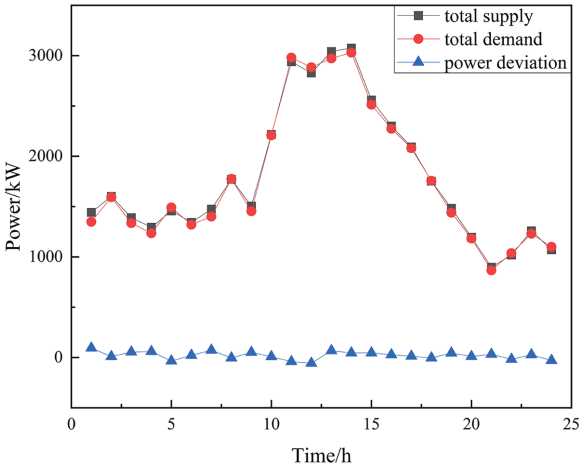


Figure 12: Curves of power balance.

In addition, this paper simulates the power balance under different weather conditions. The first day is sunny, the second day is cloudy, and the third day is rainy. Within 72 h, the average power deviation was 2.7 kW, and a higher deviation (6.8 kW) was observed on the third day, due to more unstable renewable energy generation. Nevertheless, the strategy maintains a supply-and-demand matching accuracy of more than 99.5% throughout the three days. The specific situation is shown in Fig. 13.

4.3 Resource Participation Analysis

The coordinated output proportion of multilevel resources in the system within 24 h under IWOA optimization is clearly shown in Fig. 14. This power generation structure is not a simple superposition of various power sources but a result of coordinated scheduling characterised by in-depth temporal and spatial coupling and dynamic complementarity.

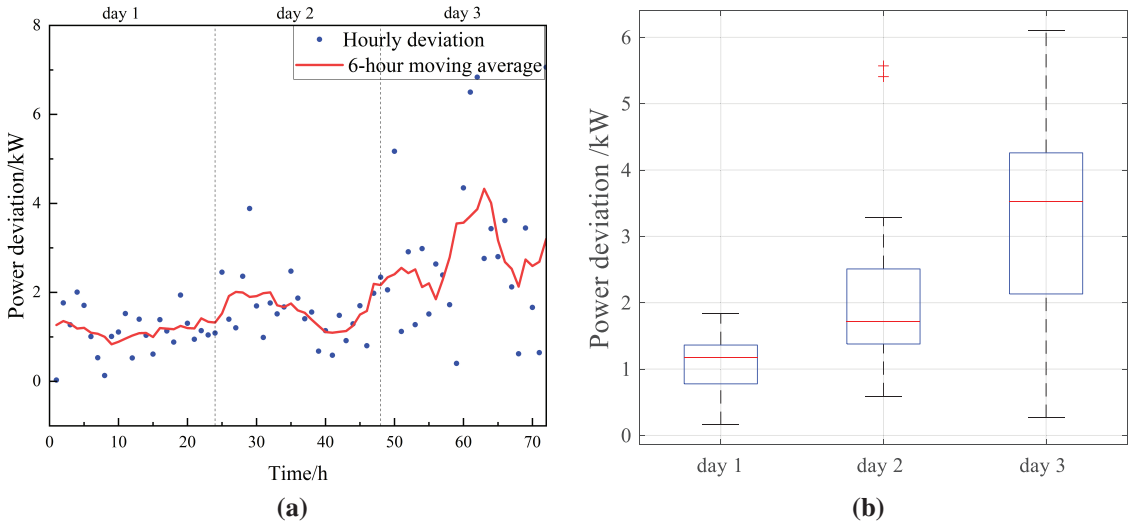


Figure 13: Situation power balance under different weather conditions: (**a**) 72 h power deviation; (**b**) Statistical distribution of daily power deviation.

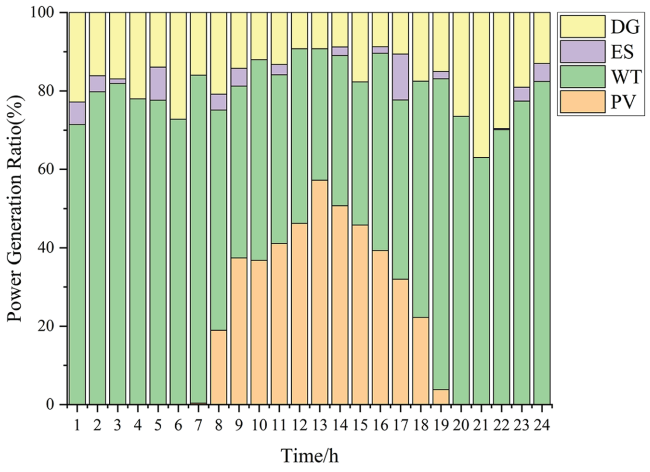


Figure 14: Multilevel resource participation.

DGs maintain high output during the nighttime, morning, and evening peak periods, assuming that the base-load supply and power guarantee are responsible. However, during the day, when PV output increases, the proportion of power generation is proactively and significantly decreased. This creates conditions to increase PV output, which has the lowest core cost, and to achieve capacity coordination and electricity substitution between traditional energy and renewable energy. The orderly charging of EVs is accurately aligned with the noon and night trough periods, when DGs need to provide support and PVs begin to decline. On the one hand, this move utilises inexpensive electricity; on the other hand, by filling the load valley, the net load curve is smoothed, which indirectly stabilises the output rate of the DGs and reduces the loss of frequent adjustment.

ESS, as the core hub of coordinated scheduling, plays a role throughout the entire process. They charge when the PV output is high and total power generation is in surplus, and discharge in the evening when the PVs are exhausted and the load increases. This behaviour not only achieves peak-valley arbitrage but also

shifts the PV output in the temporal dimension, alleviating pressure on DGs during periods of steep ramping and ensuring a smooth and stable transition of the power generation structure shown in Fig. 14.

4.4 Operation Cost Analysis

The IWOA, WOA, CWO, AWOA, PSO, and GA are compared to evaluate the operational costs associated with each resource level. The results of this comparative analysis are illustrated in Fig. 15a, which clearly shows that the IWOA significantly enhances the algorithm's convergence speed. The chaotic disturbance avoids local optima through diversity optimization, and the adaptive weight increases iteration speed by dynamically adjusting the search weight, resulting in better iteration performance for IWOA than for AWOA with only an adaptive weight and CWOA with only chaos [26]. The substantial differences in final total costs among the various algorithms clearly demonstrate that the IWOA achieves optimal cost optimization performance, with a final total cost of 9.72×10^4 CNY (Fig. 15b). In conclusion, the IWOA has distinct advantages in terms of both convergence speed and global search capability in this comparison.

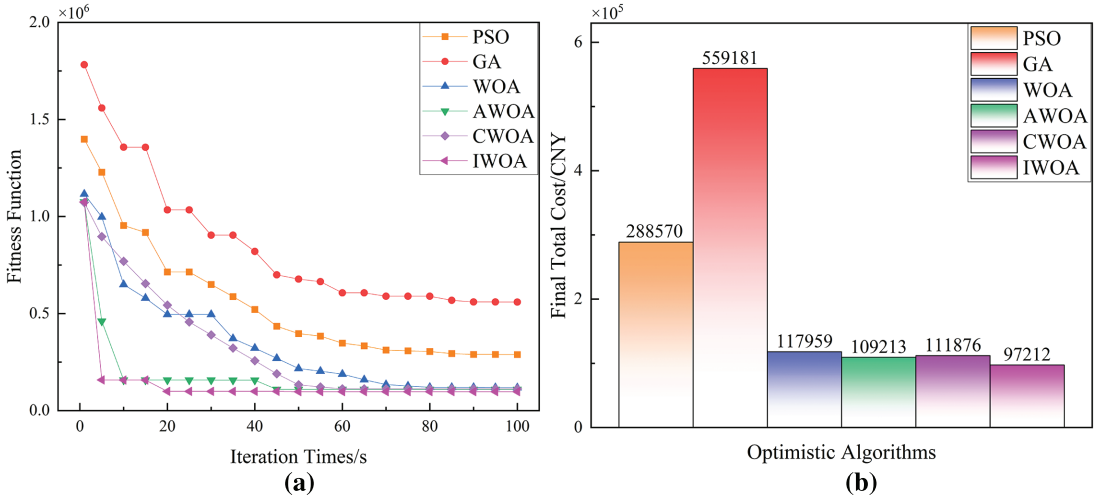


Figure 15: Comparative analysis of the different algorithms: (**a**) Convergence curves of different optimization algorithms for the solution; (**b**) Costs obtained by different optimization algorithms.

The optimized scheduling scheme is shown in Fig. 16, and the cost proportion of each resource is presented in Fig. 17. The results of the cost analysis indicate that the optimized scheduling scheme has a reasonable and efficient cost structure. The cost of DGs, which accounts for the largest share, is effectively controlled at 48.2% through IWOA. Their output curve forms a dynamic complementarity with renewable energy, significantly reducing fossil fuel consumption by 15%. Moreover, by orderly guiding the charging load of EVs to off-peak periods, an 18% cost savings is achieved, and the system's dependence on high-cost peak-shaving resources is reduced. The low operation and maintenance costs of renewable energy (8.3% for photovoltaics and 6.1% for wind power) and the low proportion of curtailment costs (3.8%) demonstrate the IWOA's excellent ability to increase the consumption of clean energy. In addition, although the ESS incurs certain expenses, the indirect benefits from its peak-valley arbitrage make it a key link in achieving overall cost optimization. The cost before and after multilevel resource optimization is shown in Table 4.

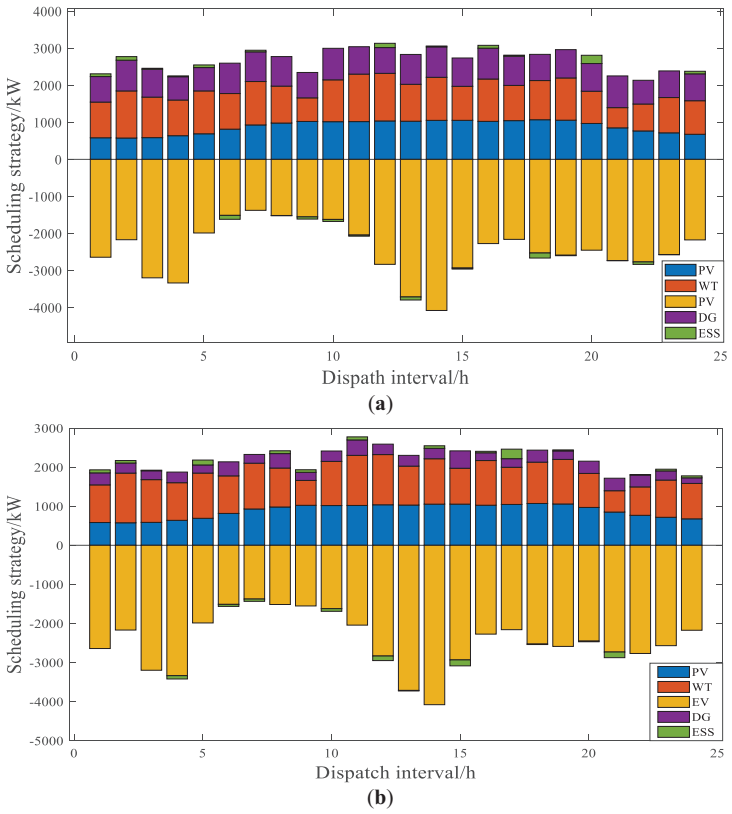


Figure 16: Optimized scheduling scheme: (**a**) Multilevel resource scheduling strategy before optimization; (**b**) Multilevel resource scheduling strategy after optimization.

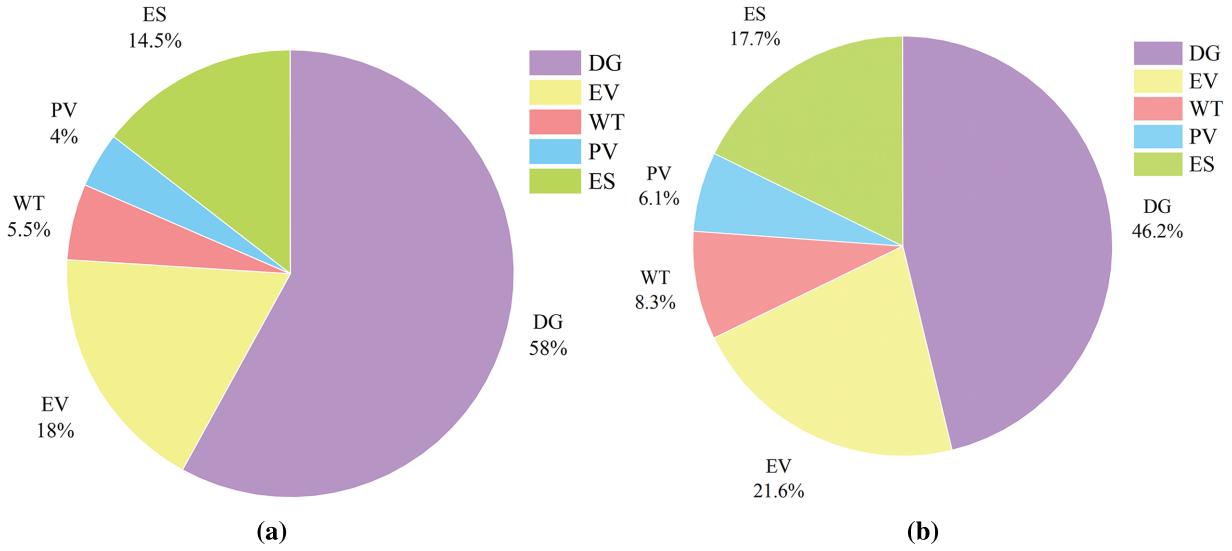


Figure 17: Cost proportion of each resource: (**a**) Proportion of multilevel resource operation costs before optimization; (**b**) Proportion of multilevel resource operation costs after optimization.

Table 4: Cost before and after multilevel resource optimization.

Resources	Costs Before Optimization (CNY)	Costs After Optimization (CNY)
DG	64,960	44,806.4
EV	20,160	20,995.2
WT	6160	8067.6
PV	4480	5929.2
ESS	16,240	17,204.4

4.5 Sensitivity Analysis

To verify the robustness of the key parameters of IWOA, this paper conducted a sensitivity analysis of the system. When the chaotic control parameter m = 3.9, the algorithm obtains the lowest total cost. When m deviates from this optimal value, the cost gradually increases, indicating that m is stable in the range of 3.8–4.0, as shown in Fig. 18. Similarly, when the perturbation probability is 10%, the optimal balance is reached. If the perturbation probability is too high, it leads to random search, and if it is too low, it is difficult to escape a local optimum. The adaptive weight w, in the range [0.4, 0.9], provides the best balance between exploration and development. These parameter settings are consistent with the recommendations of the literature [25,26], ensuring the robust performance of IWOA.

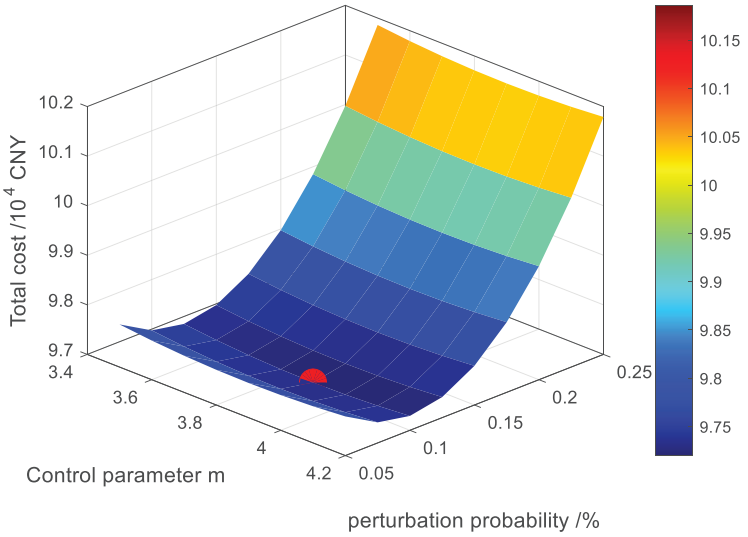


Figure 18: Double sensitivity analysis of control parameters and perturbation probability.

5 Conclusions

In this paper, a multilevel resource coordination scheduling strategy based on the IWOA was proposed to address the increased operational complexity of distribution networks with a high proportion of distributed energy integration. Through simulations, several conclusions can be drawn as follows:

(1) The improved WOA could converge faster, with the total system operation cost (9.72×10^4 CNY) being significantly lower than those of the WOA, CWOA, AWOA, PSO, and GA.

(2) By the optimization process, the cost proportions of various resources were reasonable, the clean energy absorption rate was improved, fossil fuel consumption was reduced by 15%, and the cost of orderly EV charging was decreased by 18%.

(3) The accuracy of supply–demand matching exceeds 99.8%, and the power deviation was less than 5 kW, ensuring system safety and stability. This strategy can provide a feasible solution for the optimized operation of distribution systems with a high proportion of renewable energy.

Future research should consider the load-forecasting uncertainty, the randomness of renewable energy output, and more complex robust optimization or distributional robust optimization methods. Given the computational efficiency of ultra-large-scale distribution networks, further research is needed. Finally, the scope of verification should be expanded.

Acknowledgement: Not applicable.

Funding Statement: This research was funded by the Technology Project of NARI Technology Development Co., Ltd. (No. 524609240224, Research on Key Technologies of Global Energy Management for Modern Smart Distribution Network and Its Park Verification).

Author Contributions: The authors confirm contribution to the paper as follows: Data curation, Gang Gu; funding acquisition, Rongyi Niu and Chong Li; investigation, Rongyi Niu; methodology, Rongyi Niu; resources, Gang Gu; software, Rongyi Niu; supervision, Qunhui Hu; writing—original draft, Rongyi Niu; writing—review and editing, Rongyi Niu, Chong Li, Gang Gu and Qunhui Hu. All authors have read and agreed to the published version of the manuscript.

Availability of Data and Materials: The data presented in this study are available on request from the corresponding author.

Ethics Approval: Not applicable.

Conflicts of Interest: The authors declare no conflicts of interest.

References

1. Liu YQ, Chen LX, Han XQ. The key problem analysis on the alternative new energy under the energy transition. Proc CSEE. 2022;42(2):515–24. (In Chinese). doi:10.13334/j.0258-8013.pcsee.210336.
2. Prasad M, Rather ZH, Razzaghi R, Doolla S. A new approach to determine feasible operating region of unbalanced distribution networks with distributed photovoltaics. IEEE Trans Power Deliv. 2025;40(3):1493–504. doi:10.1109/TPWRD.2025.3555210.
3. Wang C, Liu C, Zhou X, Li Y, Zhang G. Hierarchical optimal dispatch of active distribution networks considering flexibility auxiliary service of multi-community integrated energy systems. IEEE Trans Ind Appl. 2025;61(2):2770–81. doi:10.1109/TIA.2024.3462660.
4. Song G, Ma C, Ji H, Hasanien HM, Yu J, Zhao J, et al. Bi-level supply restoration method for active distribution networks considering multi-resource coordination. J Mod Power Syst Clean Energy. 2025;13(3):967–79. doi:10.35833/MPCE.2024.000616.
5. Adham M, Keene S, Bass RB. Distributed energy resources: a systematic literature review. Energy Rep. 2025;13:1980–99. doi:10.1016/j.egyr.2025.01.026.
6. Abe CF, Dias JB, Notton G, Poggi P. Computing solar irradiance and average temperature of photovoltaic modules from the maximum power point coordinates. IEEE J Photovolt. 2020;10(2):655–63. doi:10.1109/JPHOTOV.2020.2966362.
7. Ramli MAM, Bouchekara HREH. Solving the problem of large-scale optimal scheduling of distributed energy resources in smart grids using an improved variable neighborhood search. IEEE Access. 2020;8:77321–35. doi:10.1109/ACCESS.2020.2986895.
8. Zhou J, Wen G, Lv Y, Yang T, Chen G. Distributed resource allocation over multiple interacting coalitions: a game-theoretic approach. IEEE Trans Autom Control. 2024;69(11):8128–35. doi:10.1109/TAC.2024.3411833.

9. Jiang Y, Yang Y, Tan SC, Hui SYR. Power loss minimization of parallel-connected distributed energy resources in DC microgrids using a distributed gradient algorithm-based hierarchical control. IEEE Trans Smart Grid. 2022;13(6):4538–50. doi:10.1109/TSG.2022.3185264.
10. Luo Y, Nie Q, Yang D, Zhou B. Robust optimal operation of active distribution network based on minimum confidence interval of distributed energy beta distribution. J Mod Power Syst Clean Energy. 2021;9(2):423–30. doi:10.35833/MPCE.2020.000198.
11. Hoang PH, Ozkan G, Badr PR, Papari B, Edrington CS, Zehir MA, et al. A dual distributed optimal energy management method for distribution grids with electric vehicles. IEEE Trans Intell Transport Syst. 2022;23(8):13666–77. doi:10.1109/tits.2021.3126543.
12. Liao J, Lin J, Wu G, Lai S. Collaborative optimization planning method for distribution network considering hydropower, photovoltaic, storage, and charging. IEEE Access. 2024;12:172115–24. doi:10.1109/ACCESS.2024.3487996.
13. Huang J, Yuan M, Zou Z, Sun Y. Low-carbon economic optimization scheduling in distributed energy systems considering carbon emission responsibility and demand response. Int J Electr Power Energy Syst. 2025;169:110768. doi:10.1016/j.ijepes.2025.110768.
14. Turan B, Uribe CA, Wai HT, Alizadeh M. Resilient primal-dual optimization algorithms for distributed resource allocation. IEEE Trans Control Netw Syst. 2021;8(1):282–94. doi:10.1109/TCNS.2020.3024485.
15. Su H, Su W, Che Y, Ma X, Zhao T, Ren L. Configuration and operation optimization of active distribution network based on wind-solar-hydrogen-storage integration. Energy Eng. 2025;122(11):4777–97. doi:10.32604/ee.2025.068134.
16. Chen J, Mao L, Liu Y, Wang J, Sun X. Multi-objective optimization scheduling of active distribution network considering large-scale electric vehicles based on NSGAII-NDAX algorithm. IEEE Access. 2023;11:97259–73. doi:10.1109/ACCESS.2023.3312573.
17. Xiao C, Ding M, Sun L, Chung CY. Network partition-based two-layer optimal scheduling for active distribution networks with multiple stakeholders. IEEE Trans Ind Inform. 2021;17(9):5948–60. doi:10.1109/TII.2020.3038668.
18. Zhang Z, Chen Y, Ma T, Tian H, Liu J, Zhou M, et al. Multi-type energy storage expansion planning: a review for high-penetration renewable energy integration. Renew Sustain Energy Rev. 2025;219:115853. doi:10.1016/j.rser.2025.115853.
19. Ma Y, Zhang J, Lv Q, Zhao L, Ma M, Zhou Q. Energy management strategies based on deep learning in grid-forming energy storage systems. Int J Low Carbon Technol. 2025;20:1376–82. doi:10.1093/ijlct/ctaf091.
20. Qi Y, Che Y, Liu L, Ni J, Zhang S. Optimization configuration method for grid-side grid-forming energy storage system based on genetic algorithm. Energy Eng. 2025:1–10. doi:10.32604/ee.2025.068054.
21. Li X, Wang L, Yan N, Ma R. Cooperative dispatch of distributed energy storage in distribution network with PV generation systems. IEEE Trans Appl Supercond. 2021;31(8):0604304. doi:10.1109/TASC.2021.3117750.
22. Perdana YS, Muyeen SM, Al-Durra A, Morales-Paredes HK, Simões MG. Direct connection of supercapacitor-battery hybrid storage system to the grid-tied photovoltaic system. IEEE Trans Sustain Energy. 2019;10(3):1370–9. doi:10.1109/TSTE.2018.2868073.
23. Zhao ZH, Yin YF, Wang YK, Qin KR, Xue CD. Adaptive ECG signal denoising algorithm based on the improved whale optimization algorithm. IEEE Sens J. 2024;24(21):34788–97. doi:10.1109/JSEN.2024.3422995.
24. Jia L, Wang T, Gad AG, Salem A. A weighted-sum chaotic sparrow search algorithm for interdisciplinary feature selection and data classification. Sci Rep. 2023;13(1):14061. doi:10.1038/s41598-023-38252-0.
25. Archana AN, Rajeev T. A novel electric vehicle placement index for sustaining power quality in a distribution network: proper allocation of electric vehicle charging stations. IEEE Ind Appl Mag. 2023;29(5):23–35. doi:10.1109/MIAS.2023.3264860.
26. Chen L, Wang H, Tang Y, Ma Y, Wen S, Woyeso Geda M. IWOA-optimized deep learning for bearing fault diagnosis under noisy and variable conditions. IEEE Trans Instrum Meas. 2025;74:1–18. doi:10.1109/tim.2025.3602547.